PAPER

Check for updates

Dynamic and multimodal luminescence of Mn²⁺-doped Mg₄Ga₈Ge₂O₂₀ persistent phosphor for anti-counterfeiting applications†

Guna Doke, ✱ᵃᵇ Pavels Rodionovs, ᵇ Andris Antuzevics, ᵇ Jekabs Cirulis, ᵇ
Guna Krieke, ᵃᵇ Meldra Kemere, ᵇ Aldona Beganskiene ᵃ and Aleksej Zarkov ᵃ

The study provides an in-depth analysis of the structure and luminescence properties of Mg₄Ga₈Ge₂O₂₀: Mn²⁺ (MGGO) materials, focusing particularly on their dynamic color-changing capabilities. A series of single-phase MGGO:xMn²⁺ ($0.0 \leq x \leq 0.5$ mol%) was prepared. The successful incorporation of Mn²⁺ ions was verified using electron paramagnetic resonance spectroscopy. The photoluminescence and X-ray excited optical luminescence properties demonstrated that emission can be color-tuned based on the concentration of Mn²⁺ ions, with significant color shifts between red and blue observed during excitation and decaying of persistent luminescence. The persistent luminescence properties were characterized and analyzed, revealing complex decay behaviors that suggest a combination of tunneling and thermal detrapping mechanisms. Three types of traps were identified in the MGGO materials: shallow traps associated with intrinsic defect emission, deep traps, and Ga-related hole traps linked to Mn²⁺ emission. Notably, all MGGO samples can be characterized by red thermally stimulated luminescence, regardless of the initial luminescence color. These findings indicate that MGGO materials hold significant potential for anti-counterfeiting applications due to their dynamic and multimodal luminescent properties.

1. Introduction

Counterfeiting of banknotes, documents, and artworks is a growing concern for businesses, governments, and consumers. This threat has increased the demand for anti-counterfeiting measures and encryption technologies to minimize economic losses and enhance public safety. Various technologies, such as watermarks, holograms, luminescent printing, *etc.*, have been developed to address these challenges. Among these, luminescent materials – particularly multi-stimuli-responsive ones with various optical emissions have become increasingly popular due to their low cost, ease of handling, high throughput, straightforward design, flexibility, and stability.[1–3]

Recently, multi-modal anti-counterfeiting technologies that utilize at least three luminescent modes – such as photoluminescence (PL) X-ray excited optical luminescence (XRL), persistent luminescence (PersL), thermally stimulated luminescence

(TSL), optically stimulated luminescence (OSL), and upconversion luminescence – have garnered significant interest from scientists around the world.[4–6] Numerous studies have aimed to create multi-modal anti-counterfeiting solutions by combining different fluorescent materials. However, this approach often leads to problems such as low homogeneity, higher costs, and inconsistent performance. As a result, there has been considerable interest in integrating three or more luminescent modes into a single material.[7,8]

The complex mechanism of PersL makes materials that exhibit this property ideal for advanced anti-counterfeiting applications.[1,9] PersL phosphors typically generate various TSL glow curves in a wide temperature range due to charge carrier trapping by traps with different trap depths. Additionally, PersL phosphors emit light long after the excitation source is removed, resulting in a higher signal-to-noise ratio than PL. Their ability to respond to multiple stimuli and emit in various modes makes it challenging for counterfeiters to replicate, providing strong anti-counterfeiting security. An even higher level of protection can be achieved by introducing a time dimension in anti-counterfeiting solutions, namely, using dynamic multicolor luminescence materials.

Recently, there has been a surge in studies focusing on dynamic multicolor luminescent materials that utilize PersL.

ᵃ *Institute of Chemistry, Vilnius University, Naugarduko 24, LT-03225 Vilnius, Lithuania. E-mail: guna.doke@cfi.lu.lv*

ᵇ *Institute of Solid State Physics, University of Latvia, Kengaraga 8, LV-1063, Riga, Latvia*

† Electronic supplementary information (ESI) available. See DOI: **https://doi.org/10.1039/d5tc00875a**

This journal is © The Royal Society of Chemistry 2025

J. Mater. Chem. C, 2025, **13**, 10871–10881 | **10871**

A common approach to achieving dynamic multicolor luminescence properties involves the use of self-activating materials doped with ions that exhibit different color PL and PersL compared to the host material's luminescence. For instance, in lead-doped CaZnGe$_2$O$_6$,[10] both host-related green PL and Pb^{2+}-related blue PL can be observed. The ratio of these luminescence bands changes while the material is exposed to UV light. However, once the UV light is turned off, only the red Pb^{2+} PersL remains. Other examples of dynamic multicolor luminescent materials suitable for anti-counterfeiting include manganese-doped CaSb$_2$O$_6$,[11] where self-reduction from Mn^{4+} to Mn^{2+} can be observed, and LiTa$_3$O$_8$:Pr^{3+}/Tb^{3+},[12] in which the color of the luminescence highly depends on the excitation wavelength.

Here, we report on versatile PersL material Mg$_4$Ga$_8$Ge$_2$O$_{20}$:Mn^{2+} that can be characterized by dynamic multicolor luminescence signal after excitation with X-rays and UV. This host doped with Cr^{3+} (ref. 13) and Tb^{3+} (ref. 14) has been previously reported as an efficient photochromic material and PersL phosphor for anti-counterfeiting. However, the defects responsible for PersL have not been analyzed in detail, and the spectroscopic properties of Mn^{2+} in Mg$_4$Ga$_8$Ge$_2$O$_{20}$ have not been reported previously.

2. Results and discussion

2.1. Phase and structure analysis

Mg$_4$Ga$_8$Ge$_2$O$_{20}$ crystallizes with a triclinic unit cell with the $P\bar{1}$ space group. The crystal structure is composed of corner-sharing [Ga/GeO$_4$] tetrahedra and [Mg/GaO$_6$] octahedra.

In tetrahedra, Ga^{3+} and Ge^{4+} are randomly distributed; on the other hand, there are two types of octahedra: the [MgO$_6$] octahedron, which is fully occupied by Mg^{2+}, and the [Mg/GaO$_6$] octahedron, which is shared by both Mg^{2+} and Ga^{3+} (Fig. 1a).[13,15]

Considering valence states and ionic radii for Mn^{2+} (0.66 Å; CN = 4 or 0.83 Å; CN = 6), Mg^{2+} (0.72 Å; CN = 6), Ga^{3+} (0.47 Å; CN = 4) and Ge^{4+} (0.39 Å, CN = 4), it is most likely that Mn^{2+} substitutes the octahedral Mg^{2+} crystallographic site.[16] The powder X-ray diffraction (XRD) patterns of MGGO samples are presented in Fig. 1b. The diffraction peaks are consistent with the standard data of PDF 04-013-6117.[17] No additional peaks could be detected in samples with the highest dopant content, suggesting that Mn^{2+} is incorporated in the crystalline lattice of MGGO. The Rietveld refinement confirmed the formation of single-phase Mg$_4$Ga$_8$Ge$_2$O$_{20}$ with a triclinic structure of space group $P\bar{1}$ (Fig. 1c). The Rietveld refinement data are summarized in Table S1 of the ESI.†

EPR spectra in Fig. 1d confirm the concentration-dependent incorporation of Mn^{2+} ions in the MGGO structure. A signal in the 200–500 mT range centered at *ca.* 350 mT with characteristic Mn^{2+} six-component hyperfine (HF) structure[18,19] is observed for all samples. As shown in the inset of Fig. 1d, the double-integrated (DI) signal intensity increases with Mn^{2+} ion concentration, confirming the successful incorporation of the dopant ions in MGGO. EPR spectra simulations were performed using the following spin-Hamiltonian (SH) approximation:

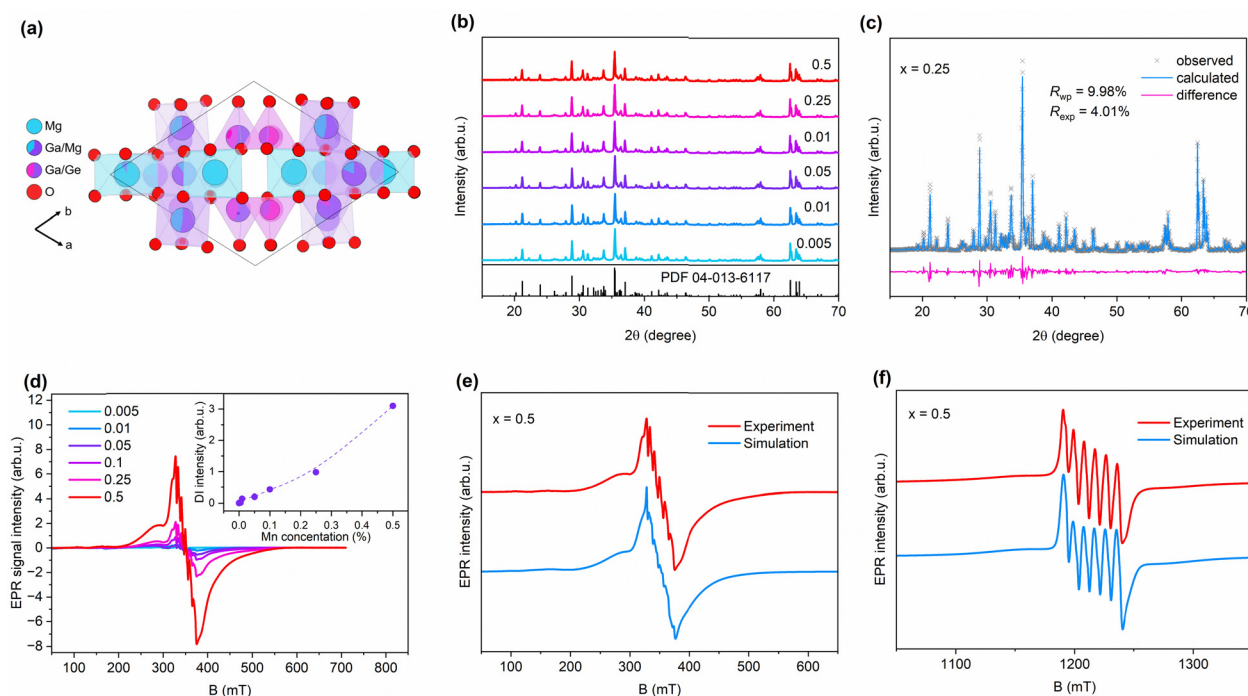$$\hat{H} = \mu_B \vec{B} g \hat{S} + \hat{S} D \hat{S} + \hat{S} A \hat{I} \qquad (1)$$

Fig. 1 (a) Crystal structure of Mg$_4$Ga$_8$Ge$_2$O$_{20}$ shown in c axis direction; (b) XRD patterns of MGGO samples; (c) Rietveld refinement plot of the x = 0.25 sample; (d) X-band EPR spectra of MGGO; inset: Double integrated (DI) EPR signal intensity as a function of Mn^{2+} concentration; EPR spectra simulations of the x = 0.5 sample recorded at (e) X-band and (f) Q-band microwave frequencies.

10872 | *J. Mater. Chem. C*, 2025, **13**, 10871–10881

This journal is © The Royal Society of Chemistry 2025

In eqn (1), g is the g-factor; μ_B – the Bohr magneton; $\vec{B}$ – external magnetic field; $\hat{S}$ – electronic spin operator; D – zero-field splitting (ZFS) parameter; A – HF coupling tensor; $\hat{I}$ – nuclear spin operator.[20] $S = 5/2$ and $I = 5/2$ are determined by the spin system (Mn^{2+}) while the SH parameters (g, A, D) are local structure-dependent and were adjusted during simulations. A reasonable fit to the experimental EPR spectra recorded at two microwave frequency bands (Fig. 1e and f) was achieved with $g = 2.00(1)$, $A = 251(1)$ MHz, and $D = 1160(100)$ MHz. It is noteworthy that despite multiple available cation sites in MGGO, the Mn^{2+} EPR spectrum can be satisfactorily simulated by a single spin system. This implies that, in the investigated concentration range, Mn^{2+} ions preferentially substitute a single crystallographic position. However, the EPR spectra are relatively broad, with the HF structure resolved for the $M_S = -1/2 \leftrightarrow M_S = +1/2$ ($\Delta M_I = 0$) transitions (330–380 mT in the X-band spectra; 1190–1240 mT in the Q-band). This observation suggests considerable structural disorder in the material, likely caused by the random occupation of several cation sites in MGGO. This effect was reproduced by incorporating a relatively broad Gaussian distribution of the ZFS parameter D in the simulations.

2.2. Photoluminescence and X-ray excited luminescence properties

Fig. 2a depicts the PL spectra of all MGGO samples and representative PLE spectra. The PLE spectra are dominated by a broad excitation band between 200–300 nm that most likely comprises Mn^{2+}–O^{2-} charge transfer and valence band (VB) to conduction band (CB) transition of the host material, as it has been previously reported for similar materials.[13,21] PL spectra, on the other hand, can be characterized by two broad luminescence bands: 600–800 nm red band typical for $^4T_1(^4G) \rightarrow {}^6A_1(^6S)$ optical transition from Mn^{2+} in the octahedral site[22,23] and 350–600 nm blue band ascribed to the host emission. Fig. S1 (ESI†) shows the PL and PLE spectra of the undoped MGGO sample, confirming the origin of the blue band. Broadband blue host emission is commonly observed in gallates and has been reported by multiple researchers.[24–27] However, the exact mechanism of luminescence in the case of interactions between various types of intrinsic defects and potentially impurity defects remains challenging to determine. Recently, Tang *et al.* published an in-depth analysis of $CaGa_4O_7$,[28] including theoretical calculations of the host's intrinsic defects and luminescence mechanisms. They concluded that electron transfer occurs from defect levels created by intrinsic defects, such as i_O, V_{Ga}, V_{GaO}, and V_O, to the ground state. Additionally, electron transfer from i_{Ga}^{2+} to i_{Ga} and from V_{O1}^{2+} to V_{O1}-related levels is also observed. These processes generate multiple overlapping emission bands that collectively contribute to the blue host emission. We believe similar processes take place in our material; however, an in-depth analysis of the intrinsic defect luminescence mechanisms in MGGO is beyond the scope of this research.
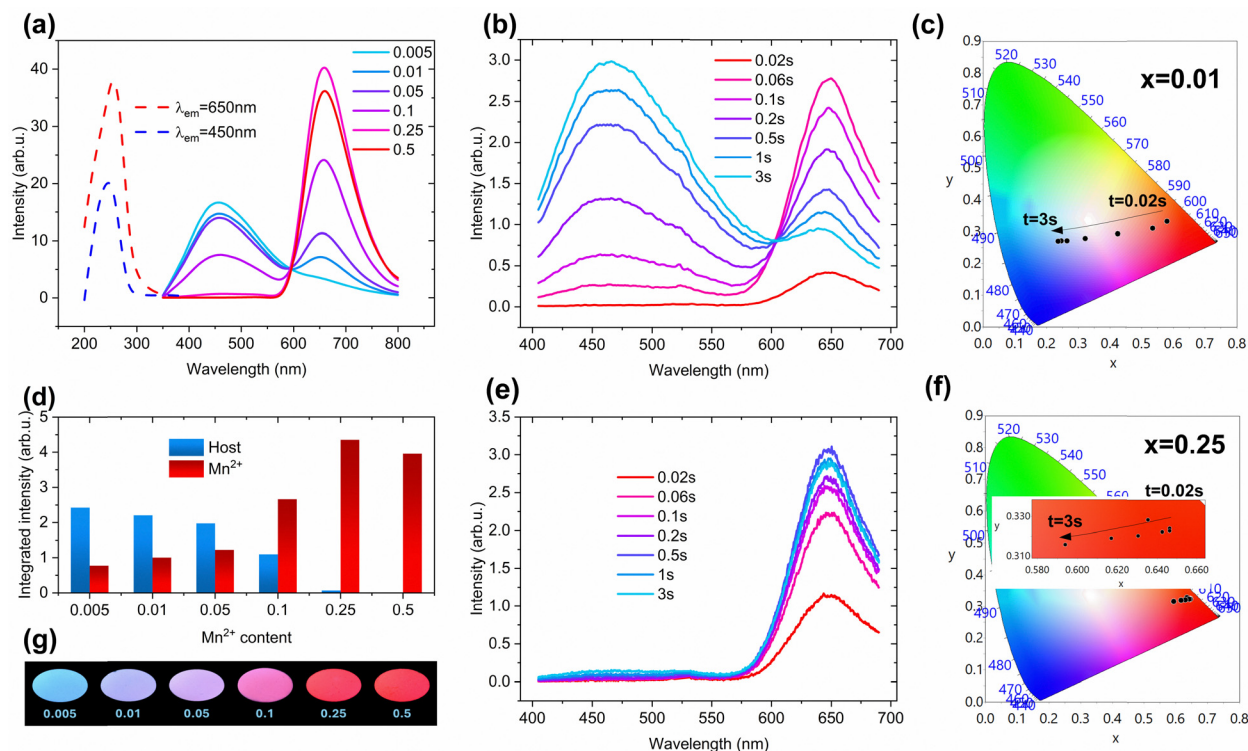

Fig. 2 (a) PLE (λ_{em} = 650, 450 nm) spectra of x = 0.05 sample (dashed lines) and PL (λ_{ex} = 254 nm) spectra of MGGO samples; (b) and (e) PL spectra of x = 0.01 and x = 0.25 samples at different periods after start of excitation; (c) and (f) dependence of the CIE 1931 chromaticity coordinates on time after start of excitation for the same samples; (d) integrated intensity of Mn^{2+} and host PL bands of MGGO samples, λ_{ex} = 254 nm, exposed until saturation; (g) digital images of the MGGO samples under UV light, the shutter speed set to $\frac{1}{4}$ s and the ISO set to1600.

The ratio of the red and blue bands is highly dependent on the content of Mn^{2+} (Fig. 2d,g), resulting in color-tunable PL with samples going through the color change from blue to violet and then to red with increased Mn^{2+} concentration. Notably, the PL of Mn^{2+} doped MGGO is not only color-tunable by Mn^{2+} concentration but also by excitation time. The PL of each sample, especially those with lower Mn^{2+} concentration, undergoes a color transition in the direction from red to blue for the first few seconds of continuous UV exposure. This effect is illustrated in Fig. 2b, c, e and f, and Fig. S2 (ESI†). Notably, when excitation begins, the red band for all samples dominates, but then a rapid increase of host luminescence and a decrease of Mn^{2+} luminescence occur until excitation saturation is reached, and the ratio of the bands no longer changes. The blue band is hardly noticeable when the Mn^{2+} concentration is 0.25 or higher; thus, no significant visual changes in these samples can be noticed. The effective PL lifetime values (τ_{eff}) related to Mn^{2+} luminescence, when excited with 254 nm light, were found to be approximately an order of magnitude higher than those of the host luminescence band. For the case where $x = 0.05$, the τ_{eff} at 650 nm is 64.7 ms, while at 450 nm, it is 6.4 ms. Additional τ_{eff} values and their corresponding PL decay profiles are presented in Table S2 and Fig. S3 (ESI†).

The same effect was observed in the case of XRL. Fig. 3 and Fig. S4 (ESI†) depict contour plots of XRL spectra when continuously excited for up to 20 min, kinetic processes of blue and red emissions, and digital images of the MGGO samples under X-rays. The dynamic nature of the red and blue bands is evident. As the concentration of Mn^{2+} increases, several observations can be made: the overall intensity of the blue band decreases, and there is a slight reduction in the saturation rate. In contrast, the saturation rate of the red band experiences a significant decline with higher Mn^{2+} concentrations. After reaching a peak, the intensity of the Mn^{2+} band begins to decrease until it stabilizes at an equilibrium point. Several factors

contribute to the dynamic changes in intensity observed in the XRL and PL bands. EPR data indicate that Mn^{2+} ions partially change their valence state upon excitation, resulting in a decrease in Mn^{2+} emission intensity. Additionally, charge tunneling between the two emitting centers and the excitation of intrinsic defects *via* charge traps may also play a role in the observed dynamic color shift in emission. The initial increase in intensity, which correlates with the concentration of Mn^{2+} ions, suggests that recombination centers are progressively filled with charges tunneling from traps as excitation begins. Moreover, the following decrease in the red band intensity and the increase in the blue band intensity are nearly mirrored, indicating that charge transfer from Mn^{2+} and the formation of blue-emitting centers happen simultaneously. Lastly, the gradual reduction in red band intensity after it peaks can be attributed to the photooxidation of Mn^{2+} ions and the reabsorption of luminescence by color centers created during excitation.[28,29] The rate of color change increases with excitation power as well; however, the power density required to achieve nearly instant saturation is relatively low, estimated to be around 70 μJ cm^{-2} (Fig. S5, ESI†).

It is documented that MGGO materials exhibit photochromism.[13,14] A slight coloration of the samples after UV or X-ray exposure was also observed in Mn^{2+} doped MGGO, which was investigated in this research (Fig. S6, ESI†). The results suggest that the photochromism in this host is likely related to the charge transfer processes in intrinsic defects.

2.3. Persistent luminescence properties

After removing both UV and X-ray radiation, MGGO material can be characterized by a strong PersL signal, which can be detected for at least 16 h (Fig. 4a and b). The $x = 0.05$ sample was determined as the most promising PersL phosphor. As demonstrated in Fig. 4c, the color of the PersL changes over time, and most of the samples, regardless of the initial state,
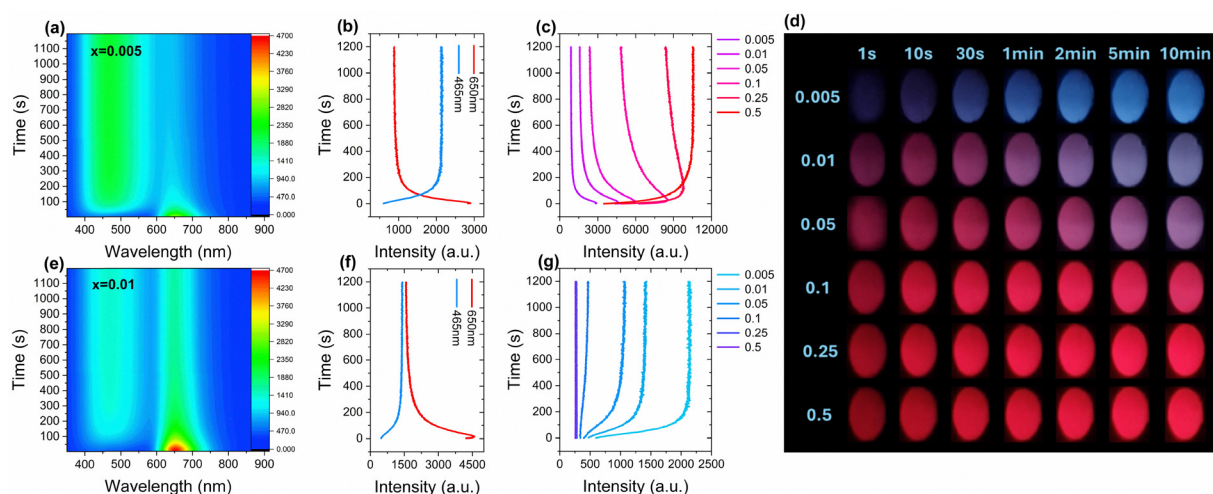

Fig. 3 (a) and (e) Contour plots of XRL spectra in continuous excitation $t = 0-20$ min of $x = 0.005$ and 0.01 samples; (b) and (f) kinetic processes for $t = 0-20$ min of 465 and 650 nm emissions under X-rays for samples $x = 0.005$ and $x = 0.01$; (c) and (g) kinetic processes of 650 nm and 450 nm XRL bands of MGGO samples; (d) digital images of the MGGO samples under X-rays in different periods after the start of excitation; the images are still frames from videos (15 fps).

glow red after the first few minutes. Fig. S7 and S8 (ESI†) demonstrate the spectral changes of the initial stages of PersL decay after irradiation with UV and X-rays, respectively. The color change is introduced with varied decay rates for the host, and the Mn^{2+}-related luminescence bands, namely, the host-related luminescence diminishes faster. PersL is a complex multi-step process; however, if other conditions are identical, the primary variable that determines the decay rate of the PersL is trap depth or activation energy E_a.[30] Therefore, different decay behaviors indicate that each type of recombination center is filled with charge carriers from different types of traps. Another explanation could be different PersL mechanisms for each luminescence band. The mechanisms in question are thermal detrapping *via* CB and tunneling directly from the trap to the recombination center. Typical PersL decay generally follows eqn (2)

$$I(t) = \frac{I_0}{(1 + \gamma t)^l} \qquad (2)$$

γ and l are fitting parameters, t is the time, and I_0 is the initial intensity. In a double-logarithmic scale, eqn (2) obeying decay kinetics appears as straight lines with a slope of $-l$. It has been shown that when the PersL mechanism is dominated by the tunneling from a trap into a random distribution of recombination centers, $l = 1$ or close to 1.[31,32] In the case of MGGO samples, the slopes of the principal part of the kinetics are close to 1 (insets of Fig. 4a and b). Thus, the presence of a tunneling mechanism in the PersL process should be considered, especially at the later stages of the PersL process, where, as previously discussed, only Mn^{2+} luminescence was observed. After UV irradiation, the $x = 0.005$ sample is an obvious outlier, showing a distinct initial faster decay. This is related to the fast-decaying blue band dominance in the spectrum at the beginning of the PersL process. If the PersL mechanism is governed by tunneling, PersL should be expected in low-temperature conditions. Fig. S9a (ESI†) shows the PersL signal at 10 K, which typically would be a clear indicator of athermal tunneling;
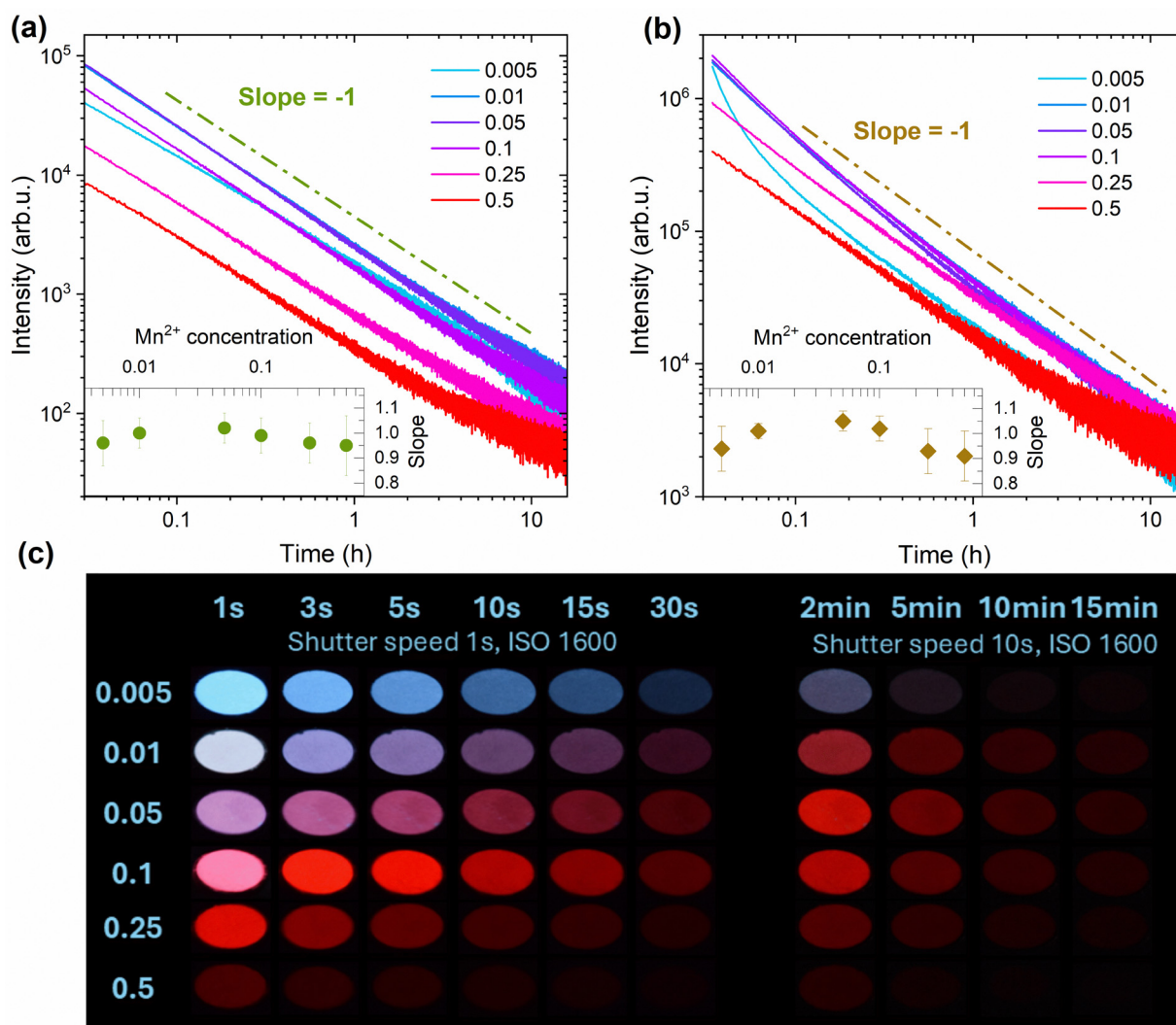

Fig. 4 The PersL decay curves of the MGGO samples after (a) irradiation with X-rays and (b) irradiation with 263 nm at room temperature. Inset: The absolute value of the slope of the linear part of the decay curves depending on Mn^{2+} content; (c) digital images of the PersL of MGGO samples at different periods after cessation of UV excitation.

This journal is © The Royal Society of Chemistry 2025

J. Mater. Chem. C, 2025, **13**, 10871–10881 | **10875**

however, in the temperature range between 10–300 K, some TSL signal can be detected as well (Fig. S9b, ESI†). Therefore, thermal detrapping from traps to CB cannot be ruled out, and the most likely PersL mechanism of MGGO materials is a combination of tunneling and classical PersL model of thermal detrapping, *i.e.*, "trap center → CB → recombination center."

2.4. Trap property analysis

To analyze the trap properties of the MGGO materials, thorough measurements were conducted using TSL and EPR techniques. Fig. 5a and d show TSL glow curves of MGGO samples irradiated with X-rays and UV, respectively. The measurements were done in the 30–350 °C temperature range, and glow curves cover most of this region with maximum intensity values around 100–200 °C. It is evident, especially in the case of UV irradiation, that glow curves consist of more than one glow peak; however, in most cases, they strongly overlap. The $x = 0.005$ sample allows for the separation of two peaks, with maxima occurring around 55 °C and 165 °C. It is important to note that the high-intensity signal observed at the beginning of the glow curves suggests two possibilities: either the actual maximum of the low-temperature peak occurs at a lower temperature, or there may be an additional glow peak present below room temperature. Fig. 6 shows a wavelength-resolved TSL contour plot of the sample with $x = 0.005$. From this, it is evident that the TSL curve can be divided into two distinct parts, with each part corresponding predominantly to different PersL bands. Specifically, the low-temperature TSL peak is associated with blue host luminescence, while the high-temperature peak corresponds to red luminescence from Mn^{2+}. Since glow peaks typically represent specific types of traps, these findings strongly suggest that the mechanisms responsible for each PersL band involve different types of traps. The upper right corner of Fig. 6 shows digital images of all
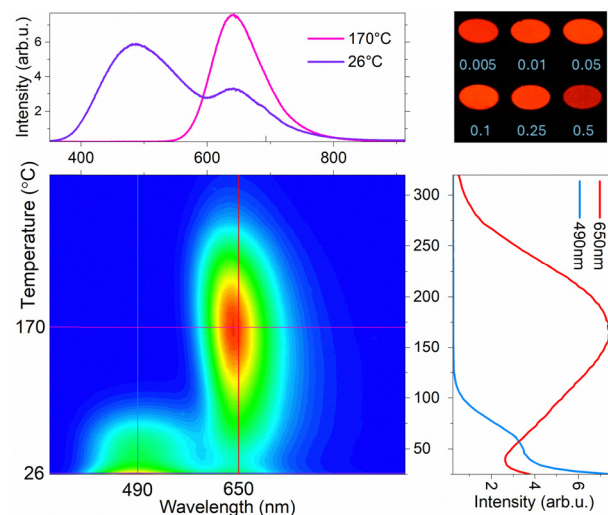

Fig. 6 Wavelength-resolved TSL contour plot of $x = 0.005$ sample; upper right corner: digital images of TSL of the MGGO samples at maximum brightness after irradiation with UV light, the shutter speed set to 2 s, and the ISO set to 1600.

samples at their maximum TSL brightness, which occurs at approximately 150 °C after being irradiated with UV light. At this temperature, all charges from shallow traps have been released, leaving only the deep traps available. As a result, all samples exhibit a similar red luminescence signal. Wavelength-resolved TSL contour plots for all samples after irradiation with both X-rays and UV light can be found in Fig. S10 (ESI†).

The best PersL sample ($x = 0.05$) was chosen for in-depth TSL analysis. For trap depth E_a determination, the T_{max}–T_{stop} method in combination with initial rise analysis (IRA) was applied. Both methods are widely acknowledged and used to
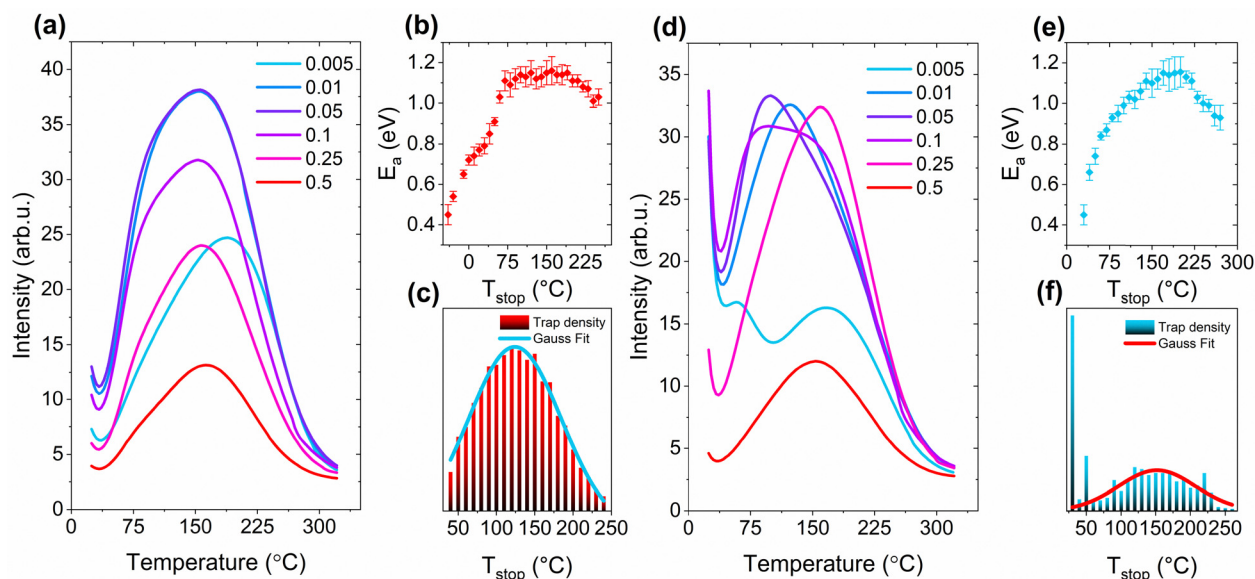

Fig. 5 (a) TSL glow curves of MGGO samples, (b) E_a values obtained by IRA, and (c) the calculated trap density distribution of the $x = 0.05$ sample after irradiation with X-rays. (d) TSL glow curves of MGGO samples, (e) E_a values obtained by IRA, and (f) the calculated trap density distribution of the $x = 0.05$ sample after irradiation with UV.

10876 | *J. Mater. Chem. C*, 2025, **13**, 10871–10881

This journal is © The Royal Society of Chemistry 2025

examine the trap properties of PersL materials.[33–35] Here, the temperature increment step used is 10 °C, and the curves obtained by the T_{max}–T_{stop} experiment are shown in Fig. S11a and c (ESI†). The E_a values are determined based on the IRA from the slopes of the linear segment of the $\ln(I) = f(1/(kT))$ plot derived from the same glow curves (Fig. S11b and d, ESI†). In the case of X-ray irradiation, an additional temperature range from −40 to 100 °C is available, and the corresponding plots are depicted in Fig. S12 (ESI†). Obtained E_a values are plotted in Fig. 5b and e. The E_a values can be categorized into two distinct groups. The initial values range from approximately 0.45 to 1.00 eV, while deeper traps show values that form a plateau around 1.15 eV. Generally, the gradually increasing values indicate a continuous distribution of traps, whereas the plateau suggests the presence of a discrete trapping site. However, the broadness of the high-temperature glow peak raises questions about the likelihood of a single trapping site. Additionally, when the T_{stop} exceeds 200 °C, a noticeable decrease in E_a values can be observed. This effect, although previously observed,[36,37] is not fully explained. The likely interpretation is that the falsely lowered E_a values result from detrapping through thermally assisted tunneling. In this scenario, the obtained E_a values represent the energy difference between the ground state and the tunneling state of a trap.[38–40] More clarity can be introduced by analyzing the filled trap density distribution.

Examining the T_{max}–T_{stop} glow curves based on the technique developed by Van den Eeckhout et al.,[41] the trap density distribution of $x = 0.05$ sample after irradiation with X-rays and UV was determined and plotted in Fig. 5c and f. The trap density distribution corresponding to measurements, where T_{stop} exceeds 50 °C regardless of the irradiation source, can be characterized with Gaussian fit. The Gaussian profile suggests that the TSL glow curve and, consequently, the PersL are generated by the detrapping of a single type of defect influenced by varying surroundings. The high structural disorder in the material is also supported by EPR experiments. It is important to note that the discussed distribution of charge traps is primarily associated with the red Mn^{2+} PersL mechanism. The shallow traps that contribute charges to the host defects responsible for blue luminescence cannot be analyzed in this way, as the corresponding glow peaks are either too close to room temperature or even below it. However, the initial bar in Fig. 5f does not conform to the Gaussian fit and represents the trap density associated with the blue PersL band.

EPR spectra measurements following UV exposure reveal slight intensity changes of Mn^{2+} dopant and unintentional Fe^{3+} impurity ions, as well as the generation of additional defect-related signals in MGGO (Fig. S13, ESI†). Qualitatively similar effects were observed after X-ray irradiation of MGGO. Three primary processes were identified: (1) Fe^{3+} EPR signal intensity decrease at ca. 160 mT; (2) Mn^{2+} intensity decrease for MGGO samples with $x \geq 0.1$; (3) generation of an additional signal centered at 350 mT related to UV-induced paramagnetic centers. The low intensity of the Fe^{3+} signal indicates that it is present in the samples in trace amounts, and it most likely

originates from precursors used in the synthesis. Fe^{3+} signal intensity reduction implies that iron ions act as electron traps undergoing partial $Fe^{3+} \rightarrow Fe^{2+}$ transformation during irradiation. The decrease of Mn^{2+} signal intensity at higher dopant concentrations could be attributed to hole-trapping processes, e.g., $Mn^{2+} \rightarrow Mn^{3+}$. The UV-generated signal was previously attributed to Cr^{5+} ions in Cr-doped MGGO;[13] however, this interpretation is dubious due to the inconsistent correlation with Cr ion concentration and the absence of EPR spectra simulation results. Furthermore, the observation of the signal in undoped MGGO in this study suggests that it is associated with intrinsic defects in the host lattice.

Fig. 7 provides a detailed analysis of the UV-induced paramagnetic center in MGGO. As shown in Fig. S14 (ESI†), qualitatively similar signals are excited in all samples, but their intensities depend on Mn^{2+} concentration, reaching a maximum in the 0.005–0.05 range (see the inset of Fig. 7a). As discussed above, the additional Mn-related hole-trapping channel could explain suppressed defect formation at higher concentrations. Multifrequency EPR spectra simulations were performed using a SH with rhombic symmetry, incorporating electron-Zeeman and HF interaction terms:

$$\hat{H} = \mu_B \vec{B} g \hat{S} + \hat{S} A \hat{I} \tag{3}$$

A single unpaired spin ($S = 1/2$) interacting with a single Ga nucleus was considered in the simulation model. Naturally abundant gallium isotopes, ^{69}Ga (60.1%) and ^{71}Ga (39.9%) have nuclear spin $I = 3/2$ and measurably different magnetic moments.[42] Consequently, the simulation spectra in Fig. 7b and c represent a statistical superposition of two orientation-averaged powder spectra with different HF splitting. The fitted SH parameters are: $g_1 = 2.023(1)$, $g_2 = 2.011(1)$, $g_3 = 2.003(1)$, $A_1^{69Ga} = 65(5)$ MHz, $A_2^{69Ga} = 76(5)$ MHz, $A_3^{69Ga} = 71(5)$ MHz.

A model for the UV-generated center in MGGO can be proposed based on the simulation results and available literature data. Several oxidation states of gallium are paramagnetic, giving rise to EPR signals after irradiation. $S = 1/2$ electron-type Ga^0 and hole-type Ga^{2+} centers reported in alkali halides[43,44] are unlikely candidates due to their HF couplings being over an order of magnitude larger than the values determined here. In contrast, Ga^{4+} ions in $KTiOPO_4$: Ga crystals exhibited considerably smaller A values.[45] While Ga^{3+} ions could potentially serve as charge traps capturing holes in MGGO, the determined g-factor values ($g_1, g_2 > g_e$; $g_3 \approx g_e$) are more consistent with the unpaired spin localized in a p-orbital. Therefore, the trapped hole can be proposed to reside on an oxygen ion adjacent to a Ga site, forming an O^- ion with a $2p^5$ electronic configuration. O^--type centers with similar g- and A-matrices have been identified in Ga_2O_3 and $LiGaO_2$ crystals.[46–48] Variations of the center can be expected depending on the stabilizing defect, typically a nearby cation vacancy or impurity that provides a positive charge deficiency relative to the perfect lattice. In the case of MGGO, the alternating occupancy of cation sites might facilitate local charge compensation for the trapped holes without additional point defects.
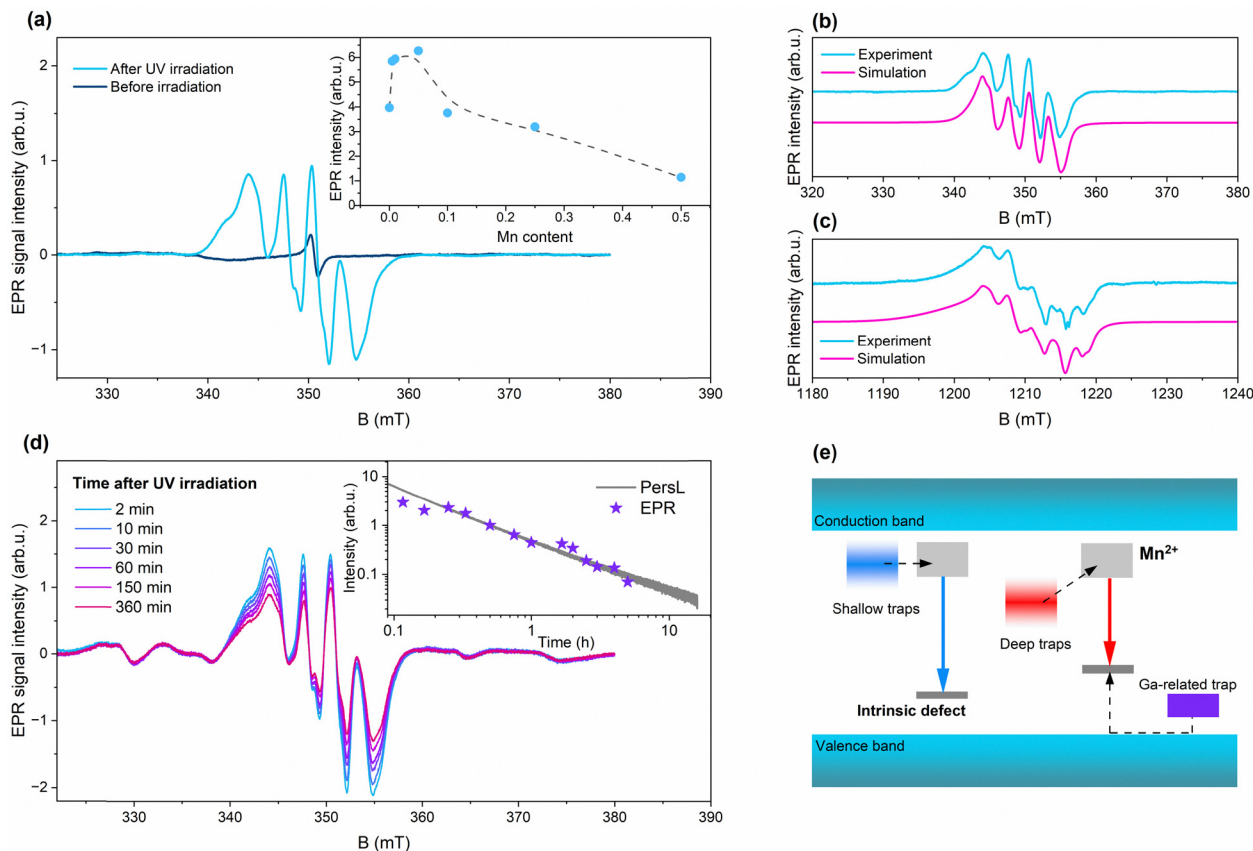
This journal is © The Royal Society of Chemistry 2025

J. Mater. Chem. C, 2025, **13**, 10871–10881 | **10877**

Fig. 7 (a) X-band EPR spectra of undoped MGGO sample before and after UV irradiation; simulations of the UV-generated EPR spectra recorded at (b) X-band and (c) Q-band microwave frequencies; (d) decay of the UV-generated EPR signal in the $x = 0.05$ sample at room temperature; inset: Comparison of EPR signal DI decay time-derivative with PersL kinetics; (e) proposed mechanism of PersL processes in MGGO.

Fig. 7d highlights the importance of the Ga-related hole centers in the PersL of MGGO. The EPR signal of UV-generated paramagnetic centers exhibits instability at room temperature, decaying to approximately 60% of the initial intensity within 5 hours. The decay rate of EPR signal DI intensity (its time-derivative) plotted in the inset of Fig. 7d is correlated with PersL kinetics. This correlation leads to the conclusion that the identified paramagnetic center is one of the charge traps enabling the PersL of MGGO.

Based on experimental evidence, we propose the PersL mechanism present in MGGO materials (Fig. 7e). During the excitation of MGGO with UV light, the Mn^{2+}–O^{2-} charge transfer band and the VB → CB transition can occur. Emission from Mn^{2+} in the red spectral range and intrinsic defect in the blue spectral range can be observed. Notably, the relative intensities of these emission bands vary during excitation, indicating energy transfer processes between the emitting centers. Possible mechanisms include photoionization of Mn^{2+}, tunneling between the two emitting centers, or excitation of intrinsic defects *via* charge traps. This dynamic interaction results in a color shift of MGGO from red to blue.

Three types of charge traps associated with PersL have been identified in this material: shallow traps linked to intrinsic defect emission, deeper charge traps associated with Mn^{2+}

emission, and Ga-related hole traps with decay rate correlated to PersL decay which predominantly represents Mn^{2+} luminescence. The PersL decay rate and charge trap properties suggest that the emitting centers are mostly filled through tunneling, especially in the case of the red Mn^{2+} band. The relative intensity of the emission bands depends on excitation conditions and Mn^{2+} content, making MGGO a versatile material with tunable PL, XRL, PersL, and TSL properties. However, further research is required to analyze the nature of the interactions between Mn^{2+} and intrinsic defects in MGGO.

2.5. Applications for the Anti-counterfeiting

Based on the previously discussed dynamic multicolor and multimodal properties of MGGO materials, we demonstrate a simple anti-counterfeiting label in Fig. 8. This label features three materials with compositions $x = 0.1$, 0.01, and 0.005, arranged in the style of a digital clock face. Under visible light (VIS), the samples appear to be the same whitish powder and cannot be distinguished, creating a visual representation of "88."

When the label is exposed to UV light, all samples glow brightly in different colors, providing no specific information. Once the UV source is turned off, each sample exhibits distinct PersL properties. The luminescence intensity of the samples
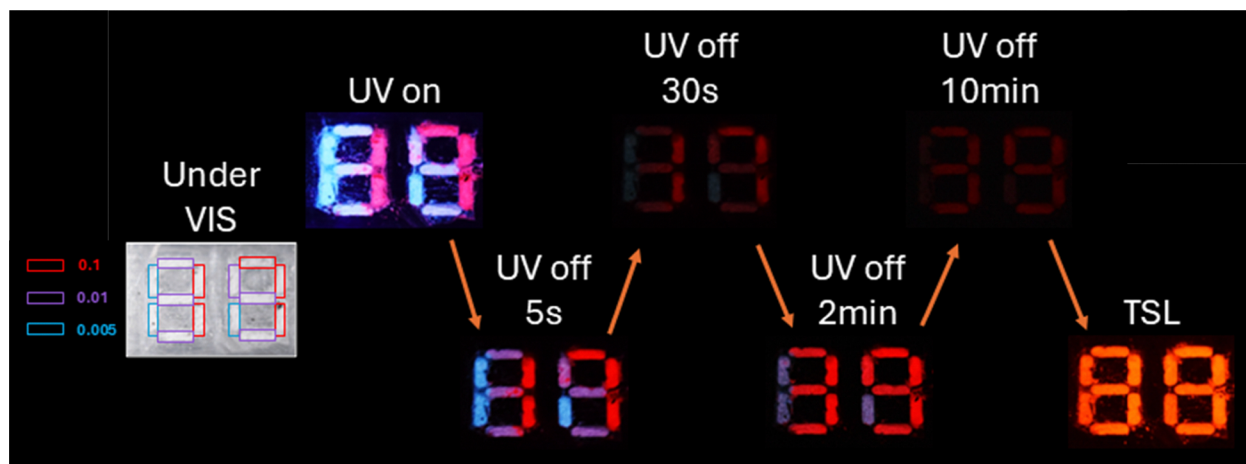
10878 | *J. Mater. Chem. C*, 2025, **13**, 10871–10881

This journal is © The Royal Society of Chemistry 2025

Fig. 8 Illustration of dynamic multicolor anticounterfeiting and information encryption. Shutter speed for images of anti-counterfeiting marking under visible light and under UV is set to 1/50 s; for UV off 5 s and 30 s, shutter speed is 1 s; for UV off 2 min, 10 min, and TSL shutter speed is 10 s, ISO 1600.

with x = 0.01 and 0.005 dims faster than that of the x = 0.1 sample. As a result, for the first few tens of seconds, an observer perceives a red number "17" on the label. After 2 minutes, the blue luminescence from the x = 0.01 sample has completely decayed, and the label then shows a red "39," which can be detected for at least 10 minutes after the UV light has been turned off. In the end, when no luminescence is visible anymore, the label is heated to reveal the TSL signal, showing a red "88". This straightforward demonstration illustrates the significant potential of MGGO materials for dynamic, multimodal, multicolor anti-counterfeiting.

3. Conclusions

In conclusion, a series of $Mg_4Ga_8Ge_2O_{20}$:x mol% Mn^{2+} (x = 0.0–0.5) samples were synthesized using the solid-state synthesis method. Upon irradiation with UV or X-rays, all doped materials exhibited a strong PersL signal detectable for at least 16 hours. Most samples demonstrated two broad luminescence bands: a blue band originating from host-related defects and a red band associated with Mn^{2+} located in an octahedral crystallographic site.

The materials displayed significant structural disorder, which resulted in a broad distribution of traps rather than discrete trap centers. Three types of traps were identified: shallow traps linked to intrinsic defect emissions, deep traps, and Ga-related hole traps associated with Mn^{2+} emission. Notably, charge tunneling from these traps to recombination centers is crucial in the PersL mechanism.

The MGGO materials exhibited tunable luminescence colors that ranged from blue to red, depending on the concentration of Mn^{2+}. Furthermore, each sample demonstrated dynamic color changes based on the excitation time and source. During PersL, most samples shifted their luminescence color, with the blue band decaying significantly faster than the red band. Conversely, the maximum TSL signal for all samples was characterized by red luminescence.

The dynamic multicolor and multimodal luminescent properties of the MGGO materials indicate significant potential for anti-counterfeiting and information encryption applications.

4. Experimental section

4.1. Preparation of phosphors

The $Mg_4Ga_8Ge_2O_{20}$:xMn (0.005 ≤ x ≤ 0.5 mol%) phosphors were synthesized *via* solid-state reaction. Stoichiometric amounts of MgO (99.99%, Thermo Fisher Scientific), Ga_2O_3 (99.999%, Thermo Fisher Scientific), GeO_2 (99.9999%, Thermo Fisher Scientific), $MnCl_2·4H_2O$ (99.99%, Alfa Aesar), and 1 wt% of H_3BO_3 (ACS, Sigma Aldrich) as a flux were mixed and thoroughly ground in an agate mortar for 20 minutes in the presence of non-polar solvent (analytically pure chloroform) that would not affect the chemical composition as a medium and ease mixing of reagents. The powder mixtures were pelletized using uniaxial press and sintered in a muffle furnace in air at 1200 °C for 12 h with a heating and cooling rate of 5 °C min^{-1}. In this research, the $Mg_4Ga_8Ge_2O_{20}$:xMn samples will be denominated as MGGO.

4.2. Measurements and characterization

Powder X-ray diffraction (XRD) patterns were measured by MiniFlex 600 RIGAKU X-ray diffractometer with an X-ray generator operating at 40 kV and 15 mA and using Cu Kα radiation. As a reference, the International Centre for Diffraction Data card for $Mg_4Ga_8Ge_2O_{20}$ (PDF 04-013-6117) was used. The crystal structure was visualized in the VESTA software[49] and Rietveld analysis was performed using Profex software.[50] X-ray fluorescence analysis was performed using an XRF X-ray analyzer, EDAX Eagle III XPL.

Photoluminescence (PL) emission and PL excitation spectra were measured using an Edinburgh Instruments FLS1000 spectrometer equipped with a CW 450 W Xe lamp as an excitation source and a Hamamatsu R928P photomultiplier tube for detection. PL spectra at different excitation times and PL decay kinetics were measured with an Andor SR-303i-B

monochromator/spectrometer coupled with a CCD camera (Andor DU-401-BV). A pulsed solid-state laser NT342/3UV from Ekspla was used as an excitation source. The quantum yield measurements were carried out with a universal measurement spectrometer Cary 7000, Agilent.

TSL curves were measured using Lexsyg research Fully Automated TL/OSL Reader from Freiberg Instruments GmbH. The irradiation sources were an X-ray tube VF-50 J s^{-1} (50 kV, 1 mA, W-anode) and a Q-switched short-pulsed UV laser DTL-389QT (263 nm) from the Laser-compact Group. TSL curves were recorded using the photomultiplier tube Hamamatsu R13456 and Andor SR-303i-B spectrometer coupled with a DV420A-BU2 CCD camera. The system is equipped with a Peltier cooling unit for the temperature range of -40–$100\ ^\circ$C. The system was operating at a linear heating rate of $1\ ^\circ$C s^{-1}.

The Bruker ELEXSYS-II E500 CW-EPR spectrometer was used for electron paramagnetic resonance (EPR) investigations of the samples. The spectra acquisition settings were the following: room temperature, 9.833 GHz (X-band) or 34.03 GHz (Q-band) microwave frequency, 10 mW microwave power, and 0.4 mT magnetic field modulation amplitude. EPR signal intensities are normalized to 100 mg of sample mass. EPR spectra simulations were performed using the open-source MATLAB toolbox – EasySpin.[51]

A digital photo camera, Nikon D3300, was used for digital images of the samples under UV light and X-rays. A mercury lamp was used to expose the samples to UV and make digital images of luminescence.

All spectral measurements, except for TSL related, were carried out at room temperature and normal atmospheric pressure in air.

Author contributions

Conceptualization (GD, AZ); data curation (GD, PR, AA, JC, GK, MK); formal analysis (GD, PR, AA, JC, GK, MK); supervision (GD, AB); visualization (GD, PR, AA, MK); writing – original draft (GD, PR, AA, GK); writing – review & editing (GD, PR, AA, JC, GK, MK, AB, AZ); sample preparation (GD, PR); funding acquisition (GD, AB).

Data availability

The data supporting this study have been included within the article and the corresponding ESI.†

Conflicts of interest

There are no conflicts to declare.

Acknowledgements

References

1 Q. Kuang, X. Hou, C. Du, X. Wang and D. Gao, *Phys. Chem. Chem. Phys.*, 2023, **25**, 17759–17768.

2 X. Yu, H. Zhang and J. Yu, *Aggregate*, 2021, **2**, 20–34.

3 C. Zhang, Q. Yin, S. Ge, J. Qi, Q. Han, W. Gao, Y. Wang, M. Zhang and J. Dong, *Mater. Res. Bull.*, 2024, **176**, 112801.

4 S. Tian, H. Zhang, X. Yang, L. Yang, Q. Min, H. Ma, X. Yu, J. Qiu and X. Xu, *Chem. Eng. J.*, 2021, **412**, 1–8.

5 Z. Wang, Z. Song, L. Ning and Q. Liu, *J. Mater. Chem. C*, 2020, **8**, 1143–1150.

6 Z. Wang, P. Pei, D. Bai, S. Zhao, X. Ma and W. Liu, *Inorg. Chem. Front.*, 2020, **7**, 2506–2514.

7 L. Hu, Y. Fan, L. Liu, X. Li, B. Zhao, R. Wang, P. Wang, A. M. El-Toni and F. Zhang, *Adv. Opt. Mater.*, 2017, **5**, 1–9.

8 Y. Liu, K. Ai and L. Lu, *Nanoscale*, 2011, **3**, 4804.

9 J. Zhang, Z. Wang, X. Huo, X. Meng, Y. Wang, H. Suo and P. Li, *Laser Photon. Rev.*, 2024, **18**, DOI: 10.1002/lpor.202300751.

10 Z. Yang, L. D. Spencer, H. Zhang, Z. L. Burmood, A. Putta and C. Jiang, *ACS Appl. Mater. Interfaces*, 2024, **16**, 16418–16426.

11 Z. Li, W. Zhang, C. Xin, Z. Chen and J. Sheng, *Ceram. Int.*, 2024, **50**, 18043–18052.

12 W. Li, R. Hu, X. Wang, Y. Li and X. Yao, *J. Alloys Compd.*, 2023, **936**, 168034.

13 Y. Jin, Y. Hu, L. Yuan, L. Chen, H. Wu, G. Ju, H. Duan and Z. Mu, *J. Mater. Chem. C*, 2016, **4**, 6614–6625.

14 F. Men, T. Hu, Z. Jiang, H. Yang, Y. Gao and Q. Zeng, *Inorg. Chem.*, 2024, **63**, 668–676.

15 J. Barbier, *Phys. Chem. Miner.*, 1990, **17**, 246–252.

16 R. D. Shannon, *Acta Crystallogr., Sect. A*, 1976, **32**, 751–767.

17 J. Barbier, *Eur. J. Mineral.*, 1998, **10**, 1283–1294.

18 E. Raudonyte-Svirbutaviciene, G. Klydziute, L. Lukaviciute, A. Antuzevics, A. Balciunaite, E. Norkus, A. Beganskiene, A. Zarkov and A. Kareiva, *Ceram. Int.*, 2024, **50**, 4005–4013.

19 A. Antuzevics, G. Krieke, G. Doke, A. Zarins, L. Avotina, E. Sprugis, J. Stadulis, A. Beganskiene, A. Kareiva and A. Zarkov, *J. Alloys Compd.*, 2024, **996**, DOI: 10.1016/j.jallcom.2024.174779.

20 J. A. Weil and J. R. Bolton, *Electron Paramagnetic Resonance*, Wiley, 2007.

21 M. Wang, X. Ming, J. Cao, L. Yang, Z. Wang, C. Ma, M. Zhang and W. Liu, *Inorg. Chem.*, 2023, **62**, 75–86.

22 Y. Liu, J. A. McLeod, L.-Y. Chang, C.-K. Chang, Y. Jiang, Z. Wang, A. Lefebvre, X. Chen and L. Liu, *Mater. Today Commun.*, 2024, **38**, 108080.

23 G. Doke, G. Krieke, A. Antuzevics, A. Sarakovskis and B. Berzina, *Opt. Mater.*, 2023, **137**, 113500.

24 P. Liu, Y. Zhang, B. Li, L. Han and Y. Xu, *Chem. Eng. J.*, 2022, **437**, 135389.

25 J. Xue, L. Li, M. Runowski, Y. Guo, B. R. Lee, J. H. Jeong, P. Du and S. H. Park, *Adv. Opt. Mater.*, 2023, **11**, DOI: 10.1002/adom.202300600.

10880 | *J. Mater. Chem. C*, 2025, **13**, 10871–10881

This journal is © The Royal Society of Chemistry 2025

26 D. Gao, P. Wang, F. Gao, W. Nguyen and W. Chen, *Nanomaterials*, 2022, **12**, 2029.

27 W. Yang, J. Li, B. Liu, X. Zhang, C. Zhang, P. Niu and X. Jiang, *Nanoscale*, 2018, **10**, 19039–19045.

28 Y. Tang, Y. Cai, K. Dou, J. Chang, W. Li, S. Wang, M. Sun, B. Huang, X. Liu, J. Qiu, L. Zhou, M. Wu and J. C. Zhang, *Nat. Commun.*, 2024, **15**, 1–16.

29 Y. Yue, T. Wang, Y. Yan, L. Guo, X. Zhu, W. Bu, G. Wang, N. Zhu, L. Zhao and X. Yu, *ACS Appl. Mater. Interfaces*, 2024, **16**, 32402–32410.

30 E. M. J. Weber, A. A. Kaminskii, M. J. Weber, M. J. Weber and M. J. Weber, *Phosphor Handbook*, CRC Press, 2018.

31 P. Avouris and T. N. Morgan, *J. Chem. Phys.*, 1981, **74**, 4347–4355.

32 A. Vedda and M. Fasoli, *Radiat. Meas.*, 2018, **118**, 86–97.

33 S. W. S. McKeever, *Phys. Status Solidi A*, 1980, **62**, 331–340.

34 V. Pagonis, G. Kitis and C. Furetta, *Numerical and practical exercises in thermoluminescence*, 2006.

35 G. Krieke, G. Doke, A. Antuzevics, R. Ignatans, I. Pudza and A. Kuzmin, *J. Alloys Compd.*, 2023, 170421.

36 S. Akca, M. Oglakci, Z. G. Portakal, N. Kucuk, M. Bakr, M. Topaksu and N. Can, *Radiat. Phys. Chem.*, 2019, **160**, 105–111.

37 K. H. Gavhane, M. S. Bhadane, A. S. Bhoir, P. P. Kulkarni, B. J. Patil, V. N. Bhoraskar, S. D. Dhole and S. S. Dahiwale, *J. Alloys Compd.*, 2020, **817**, 152805.

38 A. Vedda, M. Nikl, M. Fasoli, E. Mihokova, J. Pejchal, M. Dusek, G. Ren, C. R. Stanek, K. J. McClellan and D. D. Byler, *Phys. Rev. B:Condens. Matter Mater. Phys.*, 2008, **78**, 1–8.

39 M. Kitaura, A. Sato, K. Kamada, A. Ohnishi and M. Sasaki, *J. Appl. Phys.*, 2014, **115**, DOI: 10.1063/1.4867315.

40 F. Moretti, in *Spectroscopy for Materials Characterization*, Wiley, 2021, pp. 201–228.

41 K. Van den Eeckhout, A. J. J. Bos, D. Poelman and P. F. Smet, *Phys. Rev. B: Condens. Matter Mater. Phys.*, 2013, **87**, 045126.

42 N. C. Giles and L. E. Halliburton, in *Gallium Oxide: Technology, Devices and Applications*, Elsevier, 2018, pp. 169–190.

43 P. G. Baranov and V. A. Khramtsov, *Phys. Status Solidi B*, 1980, **101**, 153–161.

44 U. Rogulis, S. Schweizer, S. Assmann and J. M. Spaeth, *J. Appl. Phys.*, 1998, **84**, 4537–4542.

45 V. Grachev, M. Meyer, A. W. Hunt and G. Malovichko, *J. Appl. Phys.*, 2014, **116**, DOI: 10.1063/1.4903224.

46 C. A. Lenyk, M. S. Holston, B. E. Kananen, L. E. Halliburton and N. C. Giles, *J. Appl. Phys.*, 2018, **124**, DOI: 10.1063/1.5050532.

47 B. E. Kananen, L. E. Halliburton, E. M. Scherrer, K. T. Stevens, G. K. Foundos, K. B. Chang and N. C. Giles, *Appl. Phys. Lett.*, 2017, **111**, DOI: 10.1063/1.4990454.

48 B. E. Kananen, L. E. Halliburton, K. T. Stevens, G. K. Foundos and N. C. Giles, *Appl. Phys. Lett.*, 2017, **110**, DOI: 10.1063/1.4983814.

49 K. Momma and F. Izumi, *J. Appl. Crystallogr.*, 2008, **41**, 653–658.

50 N. Doebelin and R. Kleeberg, *J. Appl. Crystallogr.*, 2015, **48**, 1573–1580.

51 S. Stoll and A. Schweiger, *J. Magn. Reson.*, 2006, **178**, 42–55.

This journal is © The Royal Society of Chemistry 2025

J. Mater. Chem. C, 2025, **13**, 10871–10881 | **10881**